










ALMA resolves the first strongly-lensed Optical/NIR-dark galaxy

MARIKA GIULIETTI ^{1,2} ANDREA LAPI ^{1,3,4,5} MARCELLA MASSARDI ^{5,6,1} MERIEM BEHIRI ¹
MARTINA TORSELLO ¹ QUIRINO D'AMATO ^{1,2} TOMMASO RONCONI ^{1,7,8} FRANCESCA PERROTTA ¹ AND
ALESSANDRO BRESSAN ¹

¹SISSA, Via Bonomea 265, I-34136 Trieste, Italy

²INAF - Osservatorio di Astrofisica e Scienza dello Spazio, Via Gobetti 93/3, I-40129, Bologna, Italy

³IFPU - Institute for fundamental physics of the Universe, Via Beirut 2, 34014 Trieste, Italy

⁴INFN-Sezione di Trieste, via Valerio 2, 34127 Trieste, Italy

⁵INAF/IRA, Istituto di Radioastronomia, Via Piero Gobetti 101, 40129 Bologna, Italy

⁶INAF, Istituto di Radioastronomia - Italian ARC, Via Piero Gobetti 101, I-40129 Bologna, Italy

⁷IFPU, Via Beirut 2, I-34014 Trieste, Italy

⁸INFN-Sezione di Trieste, via Valerio 2, I-34127 Trieste, Italy

ABSTRACT

We present high-resolution ($\lesssim 0.1\text{arcsec}$) ALMA observations of the strongly-lensed galaxy HATLASJ113526.2-01460 at redshift $z \sim 3.1$ discovered in the Gama 12th field of the *Herschel*-ATLAS survey. The gravitationally lensed system is remarkably peculiar in that neither the background source nor the foreground lens show a clearly detected optical/NIR emission. We perform accurate lens modeling and source morphology reconstruction in three different (sub-)mm continuum bands, and in the C[II] and CO(8-7) spectral lines. The modeling indicates a foreground lensing (likely elliptical) galaxy with mass $\gtrsim 10^{11} M_{\odot}$ at $z \gtrsim 1.5$, while the source (sub-)mm continuum and line emissions are amplified by factors $\mu \sim 6 - 13$. We estimate extremely compact sizes $\lesssim 0.5$ kpc for the star-forming region and $\lesssim 1$ kpc for the gas component, with no clear evidence of rotation or of ongoing merging events. We perform broadband SED-fitting and retrieve the intrinsic de-magnified physical properties of the source, which is found to feature a very high star-formation rate $\gtrsim 10^3 M_{\odot} \text{ yr}^{-1}$, that given the compact sizes is on the verge of the Eddington limit for starbursts; the radio luminosity at 6 cm from available EVLA observations is consistent with the star-formation activity. The galaxy is found to be extremely rich in gas $\sim 10^{11} M_{\odot}$ and dust $\gtrsim 10^9 M_{\odot}$. The stellar content $\lesssim 10^{11} M_{\odot}$ places the source well above the main sequence of starforming galaxies, indicating that the starburst is rather young with estimated age $\sim 10^8$ yr. Our results indicate that the overall properties of HATLASJ113526.2-01460 are consistently explained by in-situ galaxy formation and evolution scenarios.

Keywords: Strong gravitational lensing (1643), High-redshift galaxies (734), Galaxy formation (595), Submillimeter astronomy (1647)

1. INTRODUCTION

Sub-millimetre galaxies (SMGs) are the main protagonists of the star formation at early cosmic times (Blain 1996, Casey et al. 2014). It is well established, that a substantial contribution at the peak of the cosmic Star Formation Rate (SFR) density comes from these heavily dust-obscured objects, featuring a sub-millimeter (sub-mm) flux density $S_{870\mu\text{m}} \gtrsim 1$ mJy and extremely high SFRs, up to $\sim 10^3 M_{\odot} \text{ yr}^{-1}$ (e.g. Simpson et al. 2020, Dudzevičiūtė et al. 2020). Because of their huge dust content these objects are heavily obscured in optical bands and extremely bright in far-infrared (FIR)/sub-

mm bands where the light of newborn stars, reprocessed by dust, is re-emitted. Moreover, SMGs have been identified as the progenitors of massive quiescent early-type galaxies and constitute the ideal laboratories to test galaxy evolutionary models. For example, in in-situ co-evolutionary scenarios (Lapi et al. 2014, 2018, Pantoni et al. 2019), the intense star formation activity is accompanied by an exponential growth of the active nucleus, whose feedback will eventually sweep away the interstellar medium. The star formation is thus stopped on a relatively short timescale while the nucleus shines as an optical quasar.

In the last years, an even more extreme population of heavily obscured SMGs has been discovered. These objects are missed in optical/near-IR (NIR) surveys and have been found up to very high redshifts ($z \sim 6$; Riechers et al. 2013, 2020, Marrone et al. 2018). These heavily obscured star-forming galaxies often lack of a counterpart even in deep NIR observed-frame Hubble Space Telescope (HST) (Wang et al. 2019, Gruppioni et al. 2020) or either show extreme red colors ($H - 3.6 \mu\text{m} > 4$; see e.g. Wang et al. 2016) and are visible only from observed-frame mid-IR(MIR) images performed e.g. with the *Spitzer*/Infrared Array Camera (IRAC). Samples of optical/NIR dark objects have been detected by observing deep CO line emission (Riechers et al. 2020), and have been efficiently selected in sensitive radio observations (Talia et al. 2021, Enia et al. 2022). These peculiar objects provide a significant and previously unknown contribution to the cosmic SFR density at $z \gtrsim 3$ estimated to be at least 10% up to 25–40% with respect to the one inferred from UV-selected populations (Wang et al. 2019, Williams et al. 2019, Gruppioni et al. 2020, Talia et al. 2021, Enia et al. 2022).

The studies conducted so far are however limited by the poor angular resolution and sensitivity in MIR/FIR and sub-mm bands, causing confusion problems and prohibiting a detailed investigation of the physical properties of optical/NIR dark galaxies and the conditions of their Interstellar Medium (ISM). In the last years, Atacama Large Millimeter/submillimeter Array (ALMA) deep field observations strongly improved the quality of the observations of high redshift dusty galaxies, detecting SMGs up to flux density limits of $S_{870\mu\text{m}} \sim 0.1 - 1$ mJy (Aravena et al. 2016, Walter et al. 2016, Dunlop et al. 2017, Franco et al. 2018, Hatsukade et al. 2018). However, even high angular resolution studies indicate that these objects are extremely compact, with typical intrinsic sizes of a few tenths of an arcsec (Pantoni et al. 2021, Massardi et al. 2017), hence very hard to resolve.

Gravitational lensing enables the observation of regions in the luminosity-redshift space of these sources, that would be otherwise unattainable with current instrumentation in reasonable integration times. The gravitational magnification of the foreground lens increases the apparent luminosity proportionally to the magnification μ and stretches the angular sizes by a factor $\sqrt{\mu}$. This behavior offers the unique possibility of studying down to sub-kpc scales the properties of objects otherwise not exceptionally bright, massive, or peculiar, and belonging to the dusty star-forming galaxy population bulk at the peak of cosmic star formation. Several works demonstrated the effectiveness of sub-mm surveys in selecting strong lensing events adopting a flux

density threshold of 100 mJy at 500 μm , in correspondence of a steep drop in the number counts of dusty star-forming galaxies at sub-mm wavelengths (Blain 1996, Negrello et al. 2010, Lapi et al. 2012) where, thanks to the magnification, they emerge as the bright tail of the population count distribution, thus minimizing the probability of possible contaminants, such as flat spectrum radio sources and low redshift spiral galaxies.

Moreover, in the FIR/sub-mm regime, while the high- z lensed dusty star-forming galaxies are particularly bright, negligible signal comes from the foreground lenses, which are often massive ellipticals at $z < 1$ that dominate the signal in optical bands. Several surveys conducted in the last decade with the *Herschel* Space Observatory led to the discovery of numerous strong lensing events. The *Herschel* Multi-tiered Extragalactic Survey (HerMES; Oliver et al. 2012) identified 11 lensed galaxies over 95 deg² (Wardlow et al. 2013); Nayyeri et al. (2016) selected other 77 candidate lensed galaxies in the HerMES Large Mode survey (HeLMS; Oliver et al. 2012) and in the *Herschel* Stripe 82 Survey (HerS; Viero et al. 2014). In particular, the *Herschel* Astrophysical Terahertz Large Area Survey (H-ATLAS; Eales et al. 2010) is the widest area (600 deg²) extragalactic survey undertaken with *Herschel* and has provided a sample of more than a hundred thousands dusty star-forming galaxies at high redshift. Among the H-ATLAS survey, a sample of 80 candidate strongly lensed dusty star-forming galaxies has been selected in Negrello et al. (2017) by means of a simple flux density selection ($S_{500\mu\text{m}} > 100$ mJy). Only 21 of them have been confirmed to be lensed thus far. Recently, another sample of 11 candidates has been selected by Ward et al. (2022) in the H-ATLAS Third Data Release conducted in the South Galactic Pole (SGP). The recent work of Shu et al. (2022) exploited lensing effects generated from galaxy clusters in order to systematically search for optically dark galaxies. Follow-ups performed with JCMT/SCUBA ($\sim 850 \mu\text{m}$) and ALMA ($\sim 870 \mu\text{m}$) for their sample reach a flux limits ~ 3 times deeper than blank fields, highlighting the capabilities of gravitational lensing in detecting even more hidden and dark objects.

In this work, we present the lens modeling, the source reconstruction, and Spectral Energy Distribution (SED) analysis of HATLASJ113526.3–014605 (J1135 hereafter), also called G12v2.43 or G12H43, an optical/NIR dark strongly lensed galaxy at $z = 3.1276$ belonging to the Negrello et al. (2017) lensed candidate sample, featuring a flux density at 500 μm amounting to 204 ± 8.6 mJy. The plan of the paper is the following: in Sect. 2 we present the target of our analysis,

and describe the archival ALMA observations and the available ancillary data in other bands; Sect. 3 and 5 describe respectively the lens modeling and source reconstruction and the SED fitting analysis; finally, we discuss and summarise our results in Sect. 6 and 7. Throughout the work, we adopt the standard flat Λ CDM cosmology (Planck Collaboration et al. 2020) with rounded parameter values: matter density $\Omega_M = 0.32$, dark energy density $\Omega_\Lambda = 0.63$, baryon density $\Omega_b = 0.05$, Hubble constant $H_0 = 100h \text{ kms}^{-1}\text{Mpc}^{-1}$ with $h = 0.67$, and mass variance $\sigma_8 = 0.81$ on a scale of $8 h^{-1} \text{ Mpc}$. At the redshift of the source 1 arcsec corresponds to 7.8 kpc .

2. THE TARGET

J1135 is part of the sample of 80 (candidate) strongly lensed galaxies (Negrello et al. 2017) located in the equatorial GAMA 12th field (RA=11:35:26, dec=-01:46:07, J2000). The spectroscopic redshift of $z = 3.1276$ of the background lensed source was obtained from blind CO searches with the Zpectrometer ultrawideband spectrometer on the Green Bank Telescope (GBT) (Haris et al. 2012) and confirmed by the Northern Extended Millimeter Array (NOEMA) observations (Yang et al. 2017). So far, no redshift measurement is available for the foreground lens. Andreani et al. (2018) presented observations of high CO transition (J=7-6) obtained with the Atacama Pathfinder EXperiment (APEX)/SEPIA band 5 receiver for the background object. From the comparison of the CO(7-6) transition with the CO(1-0) and CI(2-1) the authors pointed out to the presence of a large excitation status in the ISM of J1135.

Moreover, Vishwas et al. (2018) reported bright [OIII] $88 \mu\text{m}$ emission for J1135 detected through the z Early Universe Spectrometer (ZEUS-2) on APEX attributed to ionized hydrogen regions around massive stars. From the SED-fitting of the multi-band photometry of J1135, the authors predicted J1135 to be a young, gas-rich starburst galaxy.

The object has also been targeted by Submillimeter Array (SMA) high spatial resolution ($\sim 0.8 \text{ arcsec}$) observations described in Busmann et al. (2013), but only marginally resolved. For this reason, its lensed nature has been debated in the works described above.

2.1. ALMA observations

The object is part of low ($\lesssim 2 \text{ arcsec}$) resolution observations in band 3 (2017.1.01694.S, PI: Oteo) aimed at tracing dense molecular gas through J=4-3 transitions of HCN, HCO⁺, and HNC molecules. J1135 was also included in a project (2019.1.00663.S, PI: Butler) whose main goal was to investigate outflows in high red-

shift star-forming galaxies by tracing OH⁺ and CO(9-8) lines.

In the following, we describe the calibration, imaging and analysis of further data sets with the highest angular resolution available in the ALMA Science Archive for J1135. These spatially resolved ALMA follow-ups reveal an almost complete Einstein ring, confirming out of any doubt the lensed nature of this system.

The object has been target of ALMA Cycle 4 high-resolution follow-up in band 8 (2016.1.01371.S, PI: Amit) aimed at resolving the lensed morphology of the source and tracing the continuum at $\sim 0.7 \text{ mm}$ and the C[II] $158 \mu\text{m}$ FIR line. The continuum was observed exploiting four base-bands of width 1.98 GHz, centred at 472.284, 470.451, 460.409, 458.534 GHz and composed by 128 channels each.

We re-calibrated the raw data using the Common Astronomy Software Applications (CASA) package version 4.7.2 and running the provided calibration scripts. The continuum subtraction was manually done using the task `uvcontsub`. Imaging has been performed manually adopting a Briggs weighting scheme, which assumes a robustness factor of 0.5. The properties of the generated images are reported in Table 1, the continuum cleaned images are shown in Fig. 1, and Fig. 2 reports the C[II] channel maps rebinned in a 20 km s^{-1} interval.

The second data-set we examine is part of the ALMA Cycle 6 project (2018.1.00861.S, PI: Yang) carried out with the goal of tracing H₂O and CO (J=8-7) lines in candidate lensed galaxies at high redshift ($z \sim 2 - 4$) in band 6 and 7. Both observations are performed with the same configuration with a maximum baseline of 1397 m and four spectral windows of 1.875 GHz bandwidth and $240 \times 7.8 \text{ MHz}$ channels each. In Band 6, the H₂O(J=2_{0,2}-1_{1,1}) and CO(J=8-7) are targeted with two spectral windows respectively centered at 239.376 GHz and 223.583 GHz, while other two windows centered at 235.940 and 221.705 GHz are dedicated to continuum observations. In Band 7, two spectral windows, centered at 281.766 and 292.621 GHz, target the H₂O(J=3_{2,1}-3_{1,2}) and H₂O(J=4_{2,2}-4_{1,3}) lines, while continuum is observed in two windows centered at 280.314 and 294.266 GHz.

Calibration is performed running the available pipeline scripts in CASA version 5.4.0-68. Imaging is performed manually adopting a Briggs weighting scheme in both band 6 and 7, with robustness parameter equal to 0.5. We image the CO(8-7) line performing an automatic continuum-subtraction. Fig 3 reports the CO(8-7) channel maps obtained performing imaging with a channel width of 20 km s^{-1} .

The main features of the ALMA data analysed in this work and the properties of the final images are reported in Table 1. Note that H₂O data cubes included in Cycle 6 observations will not be analysed in this paper.

2.2. Data analysis

The flux densities derived for the continuum emission of the lensed source are reported in Tab. 3. We also include the flux density value measured from the archival image of the Band 3 continuum emission mentioned in Sect. 2. Flux density uncertainties are computed including a 5% estimation of the flux calibration accuracy:

$$\delta S_{\text{image}} = \sqrt{(\sigma_{\text{image}})^2 + (0.05 \times S_{\text{image}})^2}, \quad (1)$$

with σ_{image} being the image noise.

By fitting the resolved ALMA spectral lines with a single Gaussian profile we obtain the full-width half maximum (FWHM) values for both CO(8-7) and C[II] lines corresponding to $215. \pm 4$ and 181 ± 5 km s⁻¹ respectively, in concordance to what is found by GBT and NOEMA CO and H₂O lines analysed in Harris et al. (2012) and Yang et al. (2017). The peak is detected at $\nu_{\text{obs}} = 460.504 \pm 0.003$ GHz for C[II] and $\nu_{\text{obs}} = 223.356 \pm 0.0011$ GHz for the CO(8-7), confirming the redshift estimate by Harris et al. (2012) of 3.127 whose associated uncertainties are $\delta z_{\text{C[II]}} = \pm 0.005$ and $\delta z_{\text{CO(8-7)}} = \pm 0.003$ respectively. The observed magnified line profiles measured within a region containing the whole source emission are shown in Fig. 4. Following Carilli & Walter (2013) we compute the observed magnified C[II] and CO(8-7) luminosities expressed in units of K km s⁻¹ as:

$$L'_{\text{line}} = 3.25 \times 10^7 \times S_{\text{line}} \Delta v \frac{D_L^2}{(1+z)^3 \nu_{\text{obs}}^2}. \quad (2)$$

Where $S_{\text{line}} \Delta v$ is the measured flux of the line profile (in units of Jy km s⁻¹) and D_L is the luminosity distance. The luminosities expressed in L_{\odot} are computed as $L_{\text{line}} = 3 \times 10^{-11} \nu_{\text{rest}}^3 L'_{\text{line}}$. The final values computed the C[II] and the CO(8-7) lines are summarised in Table 2.

2.3. Other bands

J1135 is covered by several surveys, such as the Kilo-Degree Survey (KiDS, de Jong et al. 2013) and the Hyper Suprime-Cam Subaru Strategic Program in the UV/optical bands (Aihara et al. 2018, 2022), the VISTA Kilo-degree Infrared Galaxy Public Survey (VIKING, Edge et al. 2013), and the UK Infrared Deep Sky Survey Large Area Survey (UKIDSS-LAS, Lawrence et al.

2007) surveys in the Near-IR (NIR), the Wide-field Infrared Survey Explorer (WISE, Wright et al. 2010) in the MIR. PACS and SPIRE FIR observations are reported in HATLAS First and Second Data Release catalogues (Valiante et al. 2016, Maddox et al. 2017). Moreover, the source is covered by the VLA Faint Images of the Radio Sky at Twenty-Centimeters (FIRST, Becker et al. 1995) survey in the radio band, where no emission is detected.

High resolution NIR follow-up observations are available for J1135. The target was observed as part of the Cycle 19 HST/WFC3 snapshot program (PI: Negrello) at a wavelength of $\lambda = 1.15 \mu\text{m}$ (see Negrello et al. 2014 for further details of the observations) and with the Keck telescope in Adaptive Optics (AO) in the Ks band (Calanog et al. 2014). No successful detection has been found in the Ks image, while a marginal emission ($\lesssim 3\sigma$) is present in the HST image, however, given the un-sufficient sensitivity and angular resolution it is not possible to unambiguously confirm whether it is associated to the foreground lens or the background source.

The object is also detected in MIR observations available in the *Spitzer*/IRAC Data Archive (PI: Cooray) and described in Ma et al. (2015), covering IRAC channel 1 and channel 2, at $3.6 \mu\text{m}$ and $4.8 \mu\text{m}$ respectively.

In addition, we find EVLA radio data in the NRAO Archive, in particular follow-ups in C-band centred at ~ 6 GHz (project code: 16A-240, PI: Smith). Data are processed by running the calibration scripts, cleaning is performed manually with CASA adopting an interactive mask. The final image reaches a mean rms of ~ 0.013 mJy beam⁻¹ and a restored beam ellipse of 1.13×0.84 arcsec (see Fig. 5).

The multi-band (optical-to-mid IR) image cut-outs of J1135 are reported in Figure 6. A faint emission at $\sim 4 \sigma$ emerges starting from the VIKING H-band and is detected in both IRAC channels with a S/N $\gtrsim 6$, but the angular resolution is not sufficient to resolve any lensing-features (e.g arcs) in the NIR/MIR regime. Flux densities are estimated by performing aperture photometry with an aperture diameter of 2 arcsec for NIR VIKING images and 6 arcsec for *Spitzer*/IRAC images. Table 3 summarises the photometry for J1135, we report upper limits for non-detections (i.e. emission with S/N $\lesssim 3$).

3. LENS MODELING AND SOURCE RECONSTRUCTION

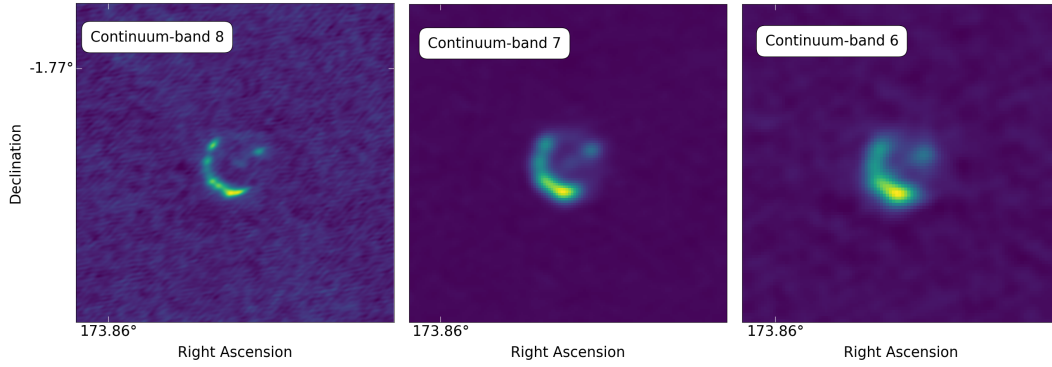
In order to reconstruct the intrinsic background source morphology we perform lens modeling analysis with the open source Python 3.6+ code *PyAutoLens* (Nightingale et al. 2018, 2021), which implements the Regularized Semi-Linear Inversion (SLI) Method described in Warren & Dye (2003) together with the adaptive source

Table 1. Overview of the ALMA observations used in this paper. H₂O lines in Cycle 6 data are not analysed in this work.

	Cycle 4 B8	Cycle 6 B6	Cycle 6 B7
Project ID	2016.1.01371.S	2018.1.00861.S	2018.1.00861.S
Spectral set-up [MHz]	4×128×15.63	4×240×7.81	4×240×7.81
Spectral resolution [kms ⁻¹]	10.17	10.48	...
Restored beam axes [arcsec ²]	0.14× 0.07	0.29×0.25	0.23×0.2
Sensitivity [mJy beam ⁻¹]	0.541	0.043	0.025
Lines	C[II]	CO(8-7)	...

Table 2. Properties of the C[II] and CO(8-7) lines. From the left: measured flux from a single Gaussian profile fit, line luminosity expressed in L_{\odot} and line luminosity expressed in K km s⁻¹pc²

Line	$\mu\Delta v S_{\text{line}}$ [Jy km s ⁻¹]	μL [10 ⁹ L _⊙]	$\mu L'$ [10 ¹¹ K km s ⁻¹ pc ²]
C[II]	82.5±2.1	27.7±0.7	1.35±0.03
CO(8-7)	9.4±0.1	1.54±0.03	0.65±0.01

**Figure 1.** ALMA band 8, 7 and 6 continuum emission for J1135.

plane pixelization scheme described in [Nightingale & Dye \(2015\)](#) adapted to interferometric data as done in [Dye et al. \(2018, 2022\)](#), [Enia et al. \(2018\)](#), [Massardi et al. \(2017\)](#), [Maresca et al. \(2022\)](#) and detailed in Appendix A.

3.1. Lens model

In reconstructing the source’s light profile we first need to assume a density profile for the mass of the foreground object. The lens is modelled as a Singular Isothermal Ellipsoid (SIE; [Kormann et al. 1994](#)), i.e. an elliptical power-law density distribution which goes as $\rho \propto r^{-\alpha}$, with r being the elliptical radius and with a fixed slope value $\alpha = 2$. The profile is described by five parameters: the Einstein radius θ_E , the lens centroid positions x_c , y_c , the first and the second ellipticity components of the elliptical coordinate system (e_x , e_y). The latter originate from two quantities: the positional angle (ϕ), defined counter-clockwise from the positive x-axis, and the factor $f = (1 - q)/(1 + q)$ where q is the ratio be-

tween the semi-major and semi-minor axis. The final expressions for the elliptical components are:

$$\begin{aligned} e_y &= f \times \sin(2\phi), \\ e_x &= f \times \cos(2\phi). \end{aligned} \quad (3)$$

PyAutoLens performs lens fitting through the nested sampling algorithm **Dynesty** ([Speagle 2020](#)) which samples the parameter space and computes the posterior probability distributions for the parameters of a given lens model.

Our searching chain consists in a first non-linear search aimed at setting priors for the lens model, this allows us to exclude regions in the parameter space corresponding to un-physical solutions where the code could get stuck. The best-fit lens model parameters are then used as priors for a second search aimed at initialising the inversion, improving the computational process. A final search is then performed to fully optimise the lens-model parameters. The fit is performed on a number of pixels delimited by a circular mask, where the ra-

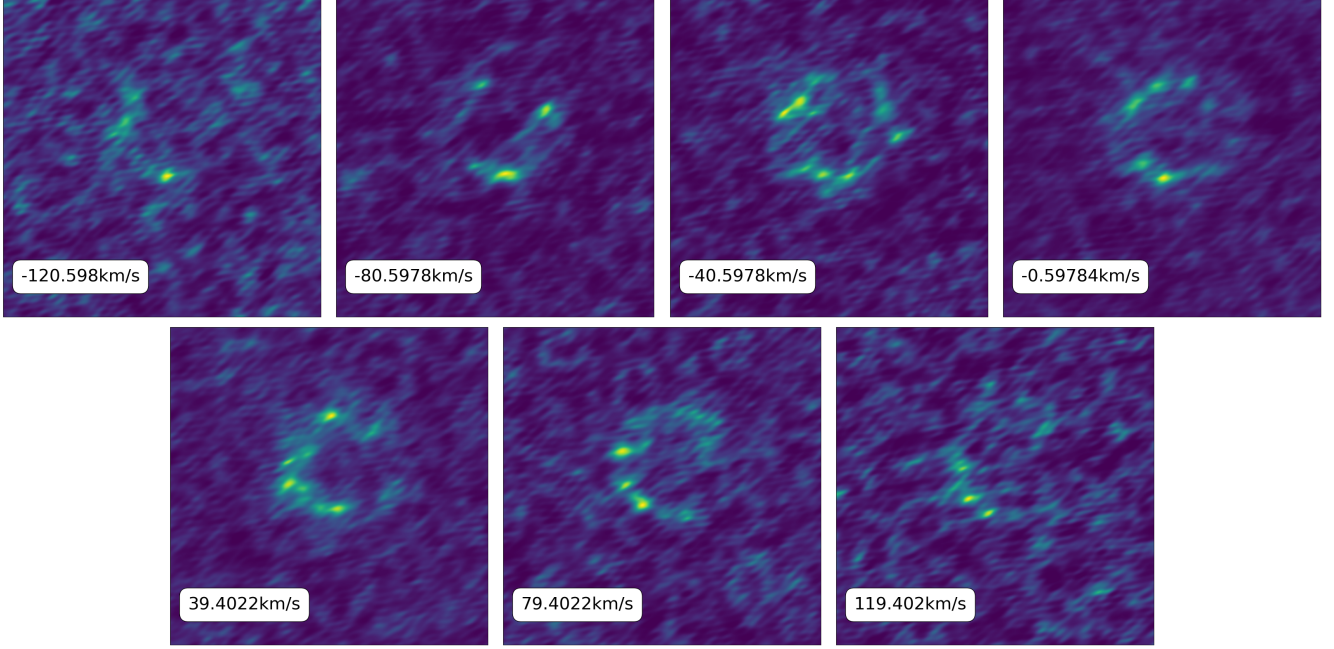


Figure 2. Channel maps and spectrum of the CII line emission for J1135.

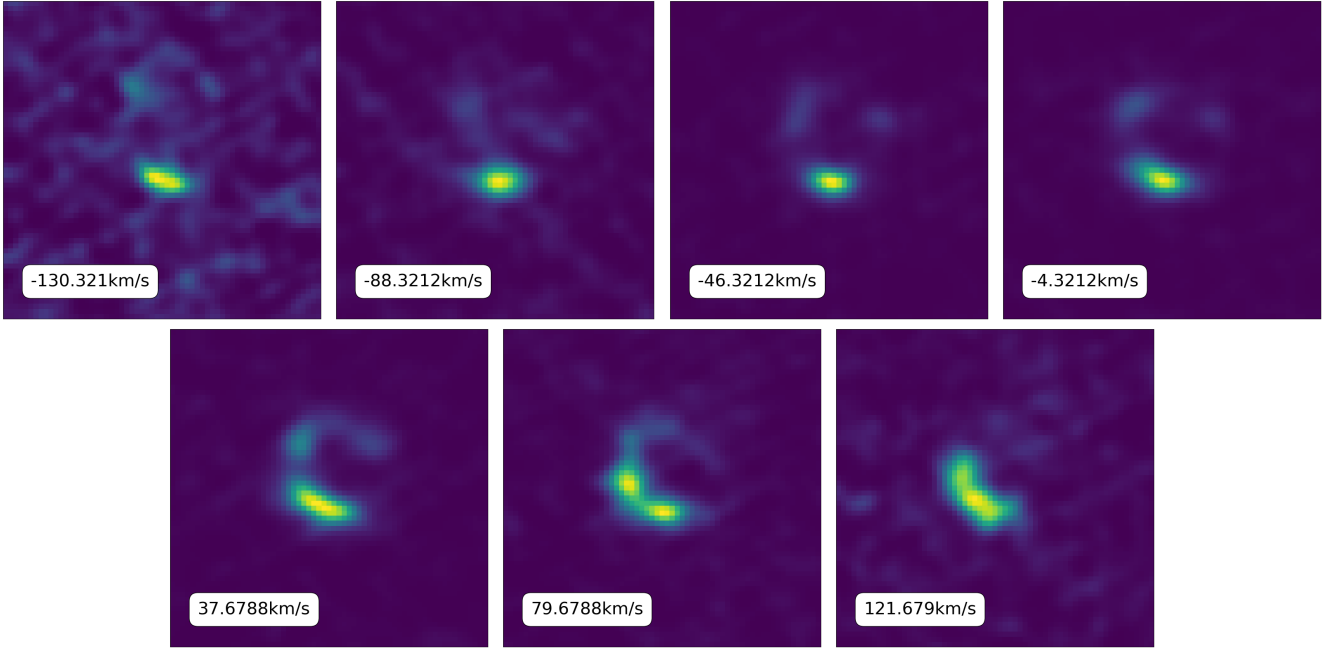


Figure 3. Channel maps of the CO(8-7) line emission for J1135.

dius changes according to the resolution of the cleaned ALMA image, in order to obtain a satisfactory fit without exceeding in terms of computational cost. The output best-fit parameters and their uncertainties are reported in Table 4. Fig. 7 and Fig. 8 shows the original lens-plane image, the model image, the residual map and the reconstructed source for the three ALMA continuum bands and the CO(8-7) and C[II] emission lines

respectively. Differences in the retrieved physical scales values reflect the heterogeneity of the data adopted in this work, which are the product of different array configurations and angular resolutions.

Moreover, we reconstruct the velocity map for the CO(8-7) line by dividing and modeling the emission in three different velocity bins. As there is no significant difference in the reconstructed emission in the bins, we

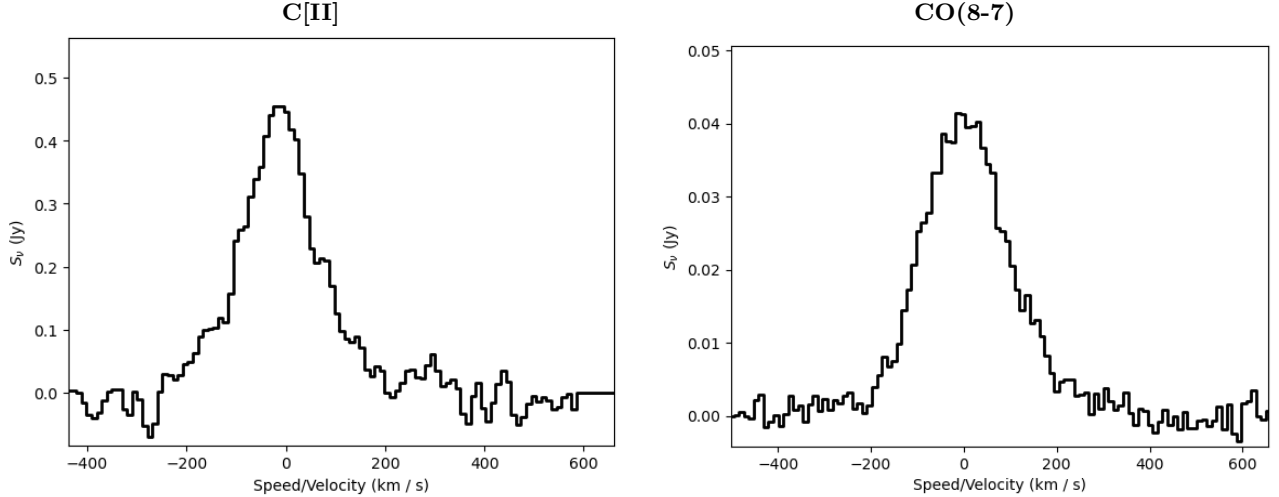


Figure 4. Spectral emission of the C[II] and CO(8-7) lines.

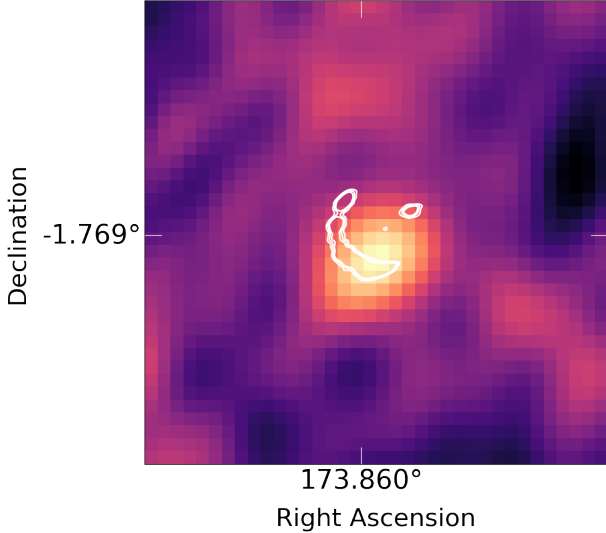


Figure 5. Image of the EVLA detection at 6 cm for J1135. White contours represent the ALMA continuum emission in band 8 at 9,7,5,3 σ

cannot claim any indication of rotation or outflow (see Fig. 9).

The resulting source physical properties are reported in Table 5. The magnification factor is computed as the ratio between the lensed and unlensed surface brightness. The effective radius is computed from the area enclosing all the pixels with signal-to-noise ratio $\gtrsim 3$ and $\gtrsim 5$ in the reconstructed source plane (SP) as $A^{SP} = \pi r_{\text{eff}}^2$. The resulting reconstructed source contains only pixels excluded from the masked lensed image area. This key information allows us to retrieve the intrinsic properties of the lensed background object.

3.2. The lens

One peculiar aspect of the J1135 gravitational lensed system is the faintness of the foreground object. Indeed, no redshift estimate is available for the lens galaxy and no clear detection is measured from the photometric images, likely due to an insufficient sensitivity and/or angular resolution. As showed in analogous studies and as revealed by HST/NIR high resolution images (e.g. Negrello et al. 2014), the foreground object usually dominates the emission in those bands, with a progressively higher contribution coming from the background source at higher wavelengths. For this reason, in order to achieve reliable results from the SED-fitting procedure, it is essential to fit and subtract the light profile of the foreground galaxy. In this case, however, only a marginal emission ($\lesssim 3\sigma$) comes from HST WFC3/F110 data and it is not possible to establish a priori whether it is originated by the lens or by the lensed object.

We therefore assume the lens to be a massive elliptical, and attribute its faintness to its relatively high redshift (e.g. $z \gtrsim 1.5$). We model the SED of the foreground object according to this assumption and constrain its luminosity by means of the Einstein (total) mass resulting from the lens modeling ($M_E \sim 1.3 \times 10^{11} M_\odot$). Specifically, we adopt the template for an elliptical galaxy with 2 Gyr age from the SWIRE library (Polletta et al. 2007). The resulting SED of this template overlapped with the photometry reported in Table 3 is showed in Fig. 10. We find the contribution from the lens to be negligible for the flux densities from the H and Ks VIKING bands up to the higher wavelengths, hence no lens-subtraction is needed. The situation is less clear for the marginal HST WFC3/F110 detection and for this reason, we consider this value as an upper limit.

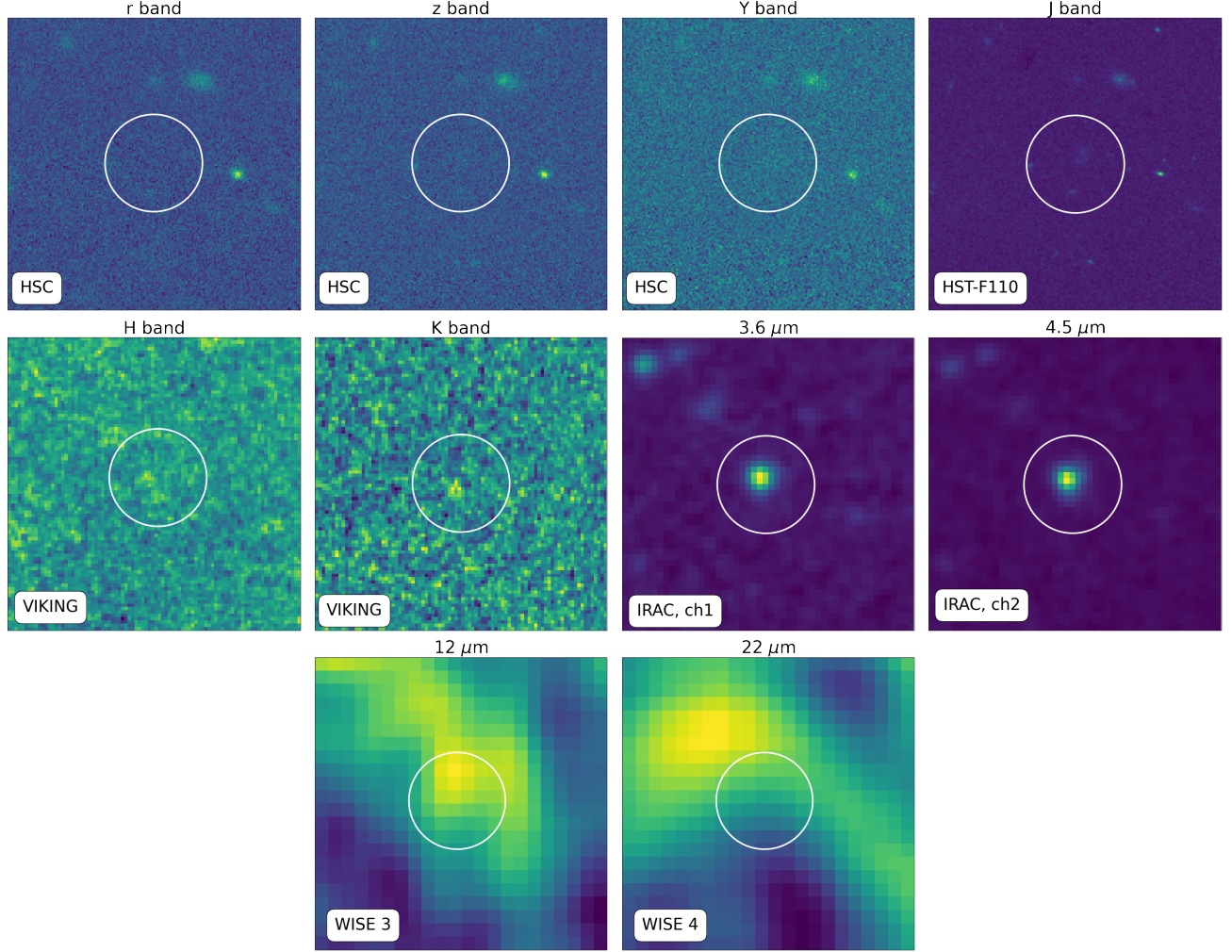


Figure 6. Cutouts of optical-to-MIR images for J1135 centred on the *Herschel* position. We plot a white circle of 5 arcsec radius for reference. The postage stamps are 30×30 arcsec

4. FAR INFRARED SED AND RADIO PROPERTIES

We compute the intrinsic Far Infrared Luminosity (FIR), defined in the wavelength range of 8-1000 μm , by de-magnifying and fitting the FIR-to-sub-mm flux densities available for G12H43. We consider the *Herschel*/PACS and *Herschel*/SPIRE photometry from the Negrello et al. (2017) sample, we include the SCUBA-2 880 μm integrated flux density reported in Bakx et al. (2018), and the flux density value measured in the 0.64, 1.04, and 1.3 mm continuum ALMA image. We use a single temperature modified black body under the optically-thin approximation, where the dust emissivity index is fixed at $\beta = 1.5$ (Nayyeri et al. 2016; Negrello et al. 2017), while the spectrum normalisation and the dust temperature (T_{dust}) are kept as free parameters. The model ($S_{\nu, \text{best}}$) which minimises the χ^2 is then integrated over the wavelength range 8-1000 μm as follows:

$$L_{\text{FIR}} = \frac{4\pi D_L^2}{(1+z)} \int_{8\mu\text{m}}^{1000\mu\text{m}} S_{\nu, \text{best}} d\nu. \quad (4)$$

The best-fit spectral energy distribution is represented in Figure 11, corresponding to a dust temperature $T_{\text{dust}} = 41.1 \pm 2.9$ K and to a resulting far infrared luminosity of $L_{\text{FIR}} = \log(L/L_{\odot}) = 12.91 \pm 0.01$.

By assuming a power law spectrum $S_{\nu} = \nu^{\alpha}$ with average radio spectral index $\alpha = -0.7 \pm 0.14$, we compute the rest-frame radio luminosity $L_{1.4\text{GHz}}$ at 1.4 GHz as:

$$L_{\nu, e} = \frac{4\pi D_L^2(z)}{(1+z)^{1+\alpha}} \left(\frac{\nu_e}{\nu_o} \right)^{\alpha} S_{\nu, o}, \quad (5)$$

where $S_{\nu, o} \propto \nu^{\alpha}$ is observed monochromatic flux density at 6 GHz corrected for a magnification factor computed as the mean of the magnification factors in output from the lens modeling of the ALMA continuum emission. ν_e and ν_o are the emitted and the observed frequency and D_L is the luminosity distance. We obtain

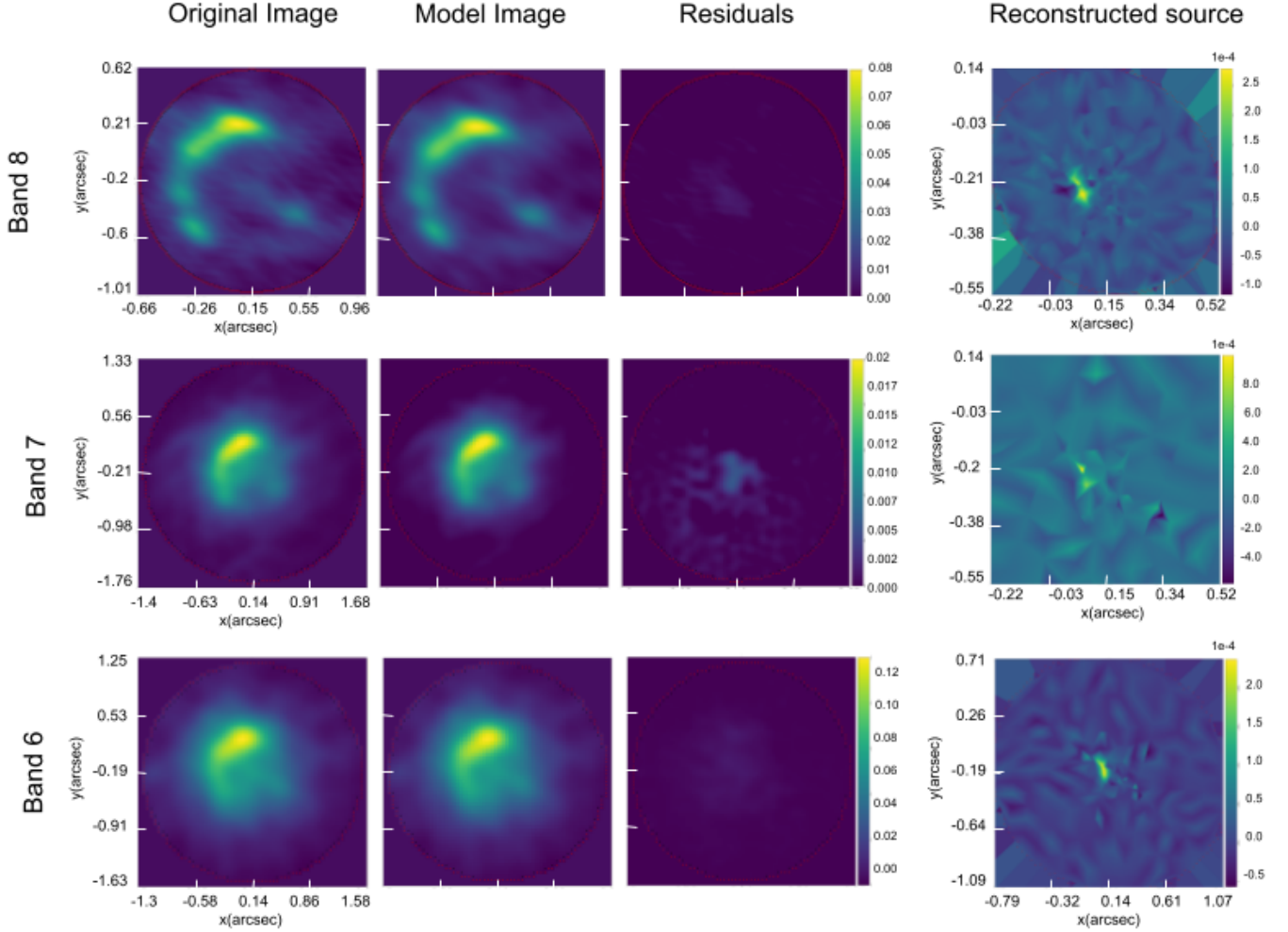


Figure 7. Results of the lens modeling and source reconstruction procedure for continuum data. From the first column to the right: the original ALMA image, the best-fit lensed model image, the fit residuals, and the reconstructed source. The colour bar indicates the surface brightness in units of Jy arcsec^{-1} . From the first row: continuum emission in bands 8, 7, and 6. Note that the y axis is inverted.

$\log L_{1.4\text{GHz}} = 24.2 \pm 0.2 \text{ W Hz}^{-1}$. Finally, we derive the far-infrared/radio correlation as:

$$q_{\text{FIR}} = \log \left(\frac{L_{\text{FIR}}[\text{W}]/3.75 \times 10^{12}}{L_{1.4\text{GHz}}[\text{W Hz}^{-1}]} \right), \quad (6)$$

inferring a value of $q_{\text{FIR}} = 2.69 \pm 0.41$.

5. SED FITTING

By correcting the available photometric information for the magnification factor we can retrieve the *intrinsic* physical properties of J1135. To achieve this goal, we perform Spectral Energy Distribution (SED) fitting with the e Code Investigating Galaxy Emission (CIGALE, Boquien et al. 2019). CIGALE is a Python SED fitting code able to reproduce broad-band uv-to-radio photometric data according to the energy balance (i.e the energy coming from the stellar uv-NIR emission is the

same as the one re-emitted by the dust in the MIR and FIR regime). The main physical properties are estimated by comparing the observed galaxy SED with the modelled one by means of a χ^2 and bayesian statistics. We exploit the available broad-band photometry described in Sect. 2.3 and the continuum ALMA emission, including a 3σ upper limit for non-detections. For low-resolution data, we correct the flux density values for the average magnification described in the previous section. As described in Sect. 3.2, we adopt the assumption that the observed photometry belongs only to the lensed source. In the following, we describe the modules adopted for the SED-fitting procedure.

The stellar emission is computed following the Bruzual & Charlot (2003) (BC03) population synthesis models, associated with a Chabrier (2003) Initial Mass Function (IMF) and metallicity values of $Z = 0.004, 0.008, 0.02$,

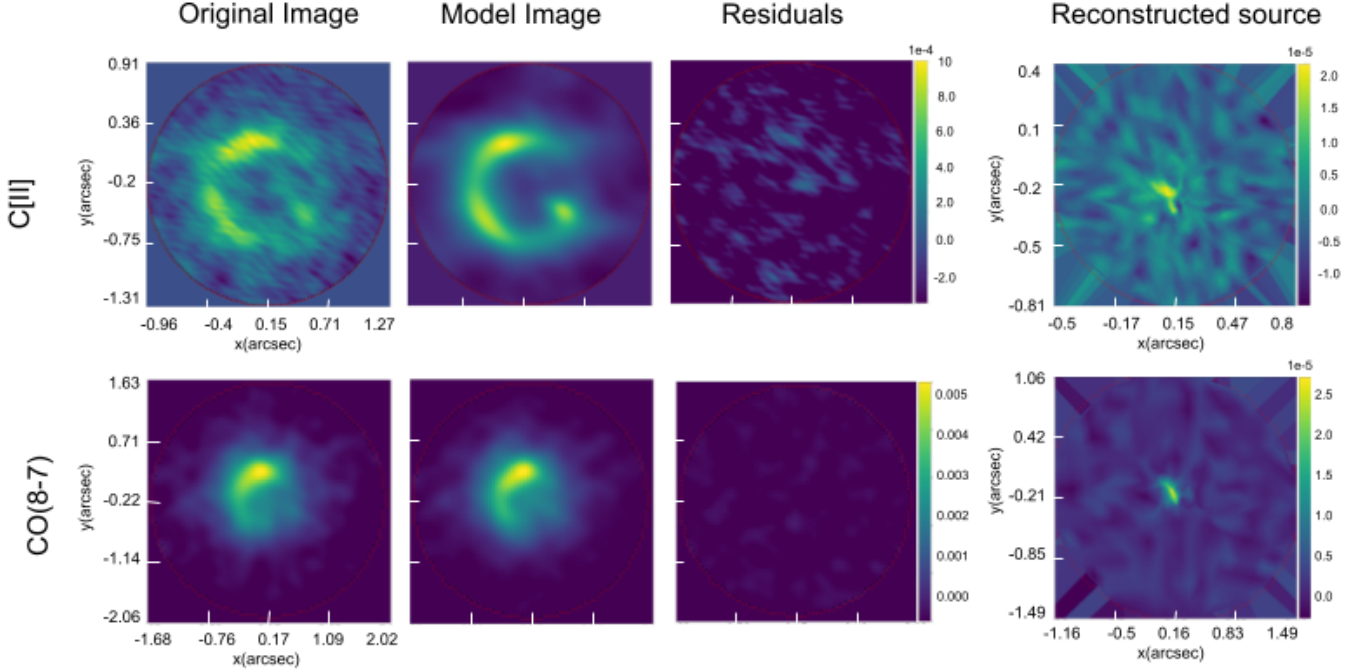


Figure 8. Same input and output as is Fig. 7 for C[II] and CO(8-7) line data, represented in the first and second row respectively.

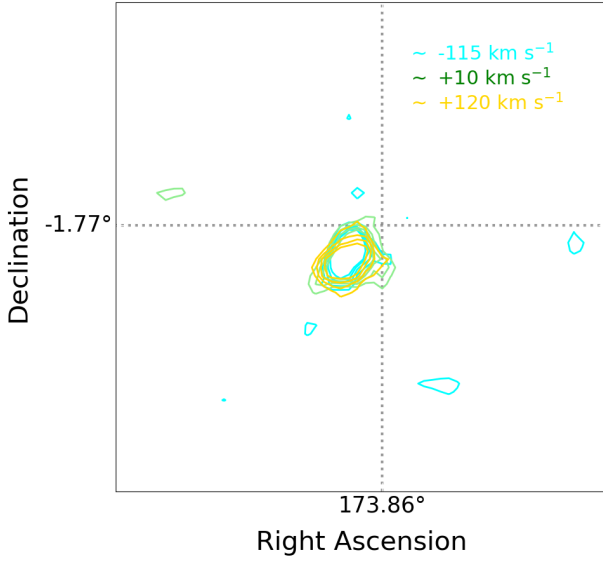


Figure 9. Reconstructed velocity map for CO(8-7) line emission. Contours represent the reconstructed surface brightness for 3 different velocity bins.

0.05. We assume a delayed star formation history, which predicts a nearly linear increase of the SFR:

$$SFR(t) \propto \frac{t}{\tau^2} \times \exp\left(-\frac{t}{\tau}\right) \quad \text{for } 0 \leq t \leq t_0, \quad (7)$$

where t_0 being the age of the onset of star formation, and τ the time at which the SFR peaks.

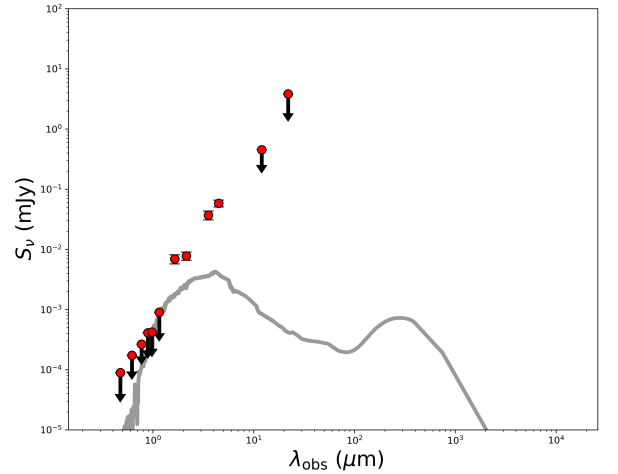


Figure 10. SED template of an passive elliptical galaxy at redshift ~ 1.5 compared with the photometry of J1135. The flux densities reported in Table 3 from HCS/g to SCUBA/850 μm are represented as red points. Upper limits at 3σ are showed as arrows.

In order to model the effect of the dust attenuation on FUV-optical light we adopt the modified Charlot & Fall (2000) prescriptions, where the attenuation is age-dependent and described by two different power-laws, one for the ISM and one for the Birth Clouds (BC).

Table 3. Photometric data for J1135. We show references for flux densities (in mJy) taken from the catalogues described in Sec 2.3 while the remaining values are extracted through aperture photometry. Upper limits are reported at the 3σ level.

Wavelength (μm)	Flux density (mJy)	Instrument
0.47	$\lesssim 0.09 \times 10^{-3}$	HSC/g
0.61	$\lesssim 0.17 \times 10^{-3}$	HSC/r
0.77	$\lesssim 0.26 \times 10^{-3}$	HSC/i
0.89	$\lesssim 0.41 \times 10^{-3}$	HSC/z
0.97	$\lesssim 0.43 \times 10^{-3}$	HSC/y
1.15	$\lesssim 0.91 \times 10^{-3}$	HST/WFC3
1.64	$(6.9 \pm 1.2) \times 10^{-3}$	VIKING/H
2.15	$(7.8 \pm 1.2) \times 10^{-3}$	VIKING/Ks
3.55	$(37.1 \pm 6.2) \times 10^{-3}$	Spitzer/IRAC1
4.49	$(58.2 \pm 7.5) \times 10^{-3}$	Spitzer/IRAC2
11.6	$\lesssim 0.45$	WISE/W3 ¹
22.1	$\lesssim 3.83$	WISE/W4 ¹
100	$\lesssim 136.3$	Herschel/PACS ²
160	151.5 ± 50.3	Herschel/PACS ²
250	278.8 ± 7.4	Herschel/SPIRE ^{2,3}
350	282.9 ± 8.2	Herschel/SPIRE ^{2,3}
500	204.0 ± 8.6	Herschel/SPIRE ^{2,3}
640	163.7 ± 7.9	ALMBA/B8
850	118.8 ± 8.5	SCUBA-2 ⁴
1043	29.4 ± 1.4	ALMA/B7
1300	16.2 ± 0.8	ALMA/B6
3450	0.71 ± 0.04	ALMA/B3
48100	0.09 ± 0.01	EVLA/BC

¹ From the WISE All-sky Data Release Wright et al. (2010)

² From the HATLAS Data Release 1 catalogue described in Valiante et al. (2016)

³ From the HATLAS Data Release 2 catalogue described in Maddox et al. (2017)

⁴ From the *Herschel* bright sources (HerBS) sample (Bakx et al. 2018)

The attenuation slopes are assumed to be -0.7 and the V-band attenuation is computed as:

$$\mu = \frac{A_{\text{V}}^{\text{ISM}}}{A_{\text{V}}^{\text{ISM}} + A_{\text{V}}^{\text{BC}}}. \quad (8)$$

In our analysis we assume $A_{\text{V}}^{\text{ISM}}$ spanning from 0.3 to 5.0 and a μ spanning from 0.3 to 0.6.

Following Draine & Li (2007), dust emission is modelled as two separated components: a diffuse one, illuminated with a single radiation field (U_{min}) originated by a general stellar population; and a second component is closely associated to regions in which the star formation occurs, heated by a variable radiation field

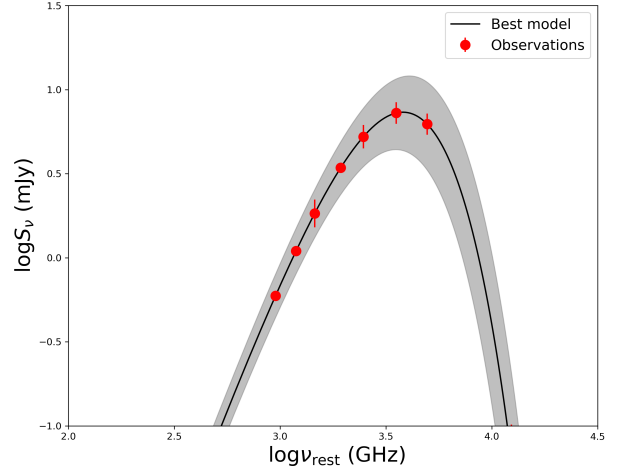


Figure 11. Best-fit FIR to sub-mm rest-frame SED of J1135. Red points are the observed flux densities and errors and the black line is the best-fitting modified black body spectrum. The grey shaded area represents the 68% confidence interval for the best-fit model.

described with a power-law profile with index α and defined between two values U_{min} and U_{max} . In particular, we use the most recent and refined version of this model which accounts also for dust-mass renormalisation (Draine et al. 2014).

The resulting value of the FIRRC parameter $q_{\text{FIR}} \sim 2.7$ computed in Sect. 4, is used as a prior for the CIGALE synchrotron module to fit radio flux density at 6 GHz assuming a fixed slope $\alpha = -0.7$ as in Eq. 5.

The best-fit model is presented in Fig. 12 and the resulting best physical properties are summarised in Table 6.

6. DISCUSSION

Taking advantage from the SED-fitting results, we are able to investigate the ISM conditions of J1135 and its evolutionary state.

6.1. Stellar and gas masses

The bunch of available data allow us to estimate the gas content by adopting several empirical calibrators. First, we directly estimate the gas mass from the C[II] following Zanella et al. (2018), we assume $\alpha_{\text{C[II]}} \equiv M_{\text{gas}}/L_{\text{C[II]}} = 22 M_{\odot}/L_{\odot}$, which is calibrated on starburst galaxies spanning a redshift range $z \sim 2-6$. Secondly, in order to estimate the molecular gas content (M_{H_2}) we derive the $L'_{\text{CO}(1-0)}$ from the de-magnified $L'_{\text{CO}(8-7)}$ luminosity. We then follow Fujimoto et al. (2022) adopting a conversion factor of $L'_{\text{CO}(1-0)} = 1.5 L'_{\text{CO}(7-6)}$ estimated for high redshift starburst galax-

Table 4. Parameters for the best-fit lens model. θ_E is the Einstein radius measured in arcsec, the lens positions are measured in arcsec and are referred to the centre of the ALMA observation. q and ϕ are the axis ratio and the positional lens angle respectively, derived from the elliptical components as described in section 3. ϕ is defined from the positive horizontal axis.

	θ_E (arcsec)	Δx_L (arcsec)	Δy_L (arcsec)	q	ϕ (deg)
Band 8	$0.460^{+0.001}_{-0.01}$	$0.163^{+0.001}_{-0.028}$	$-0.268^{+0.009}_{-0.001}$	$0.65^{+0.01}_{-0.01}$	$-33.09^{+0.02}_{-0.03}$
Band 7	$0.471^{+0.002}_{-0.010}$	$0.165^{+0.008}_{-0.012}$	$-0.252^{+0.001}_{-0.001}$	$0.62^{+0.64}_{-0.60}$	$-33.27^{+0.03}_{-0.04}$
Band 6	$0.447^{+0.001}_{-0.007}$	$0.187^{+0.001}_{-0.021}$	$-0.213^{+0.008}_{-0.001}$	$0.57^{+0.01}_{-0.01}$	$-34.09^{+0.02}_{-0.02}$
C[II]	$0.468^{+0.058}_{-0.013}$	$0.159^{+0.003}_{-0.003}$	$-0.280^{+0.027}_{-0.101}$	$0.62^{+0.19}_{-0.15}$	$-17.23^{+0.79}_{-0.70}$
CO(8-7)	$0.463^{+0.003}_{-0.001}$	$0.240^{+0.051}_{-0.067}$	$-0.209^{+0.456}_{-0.002}$	$0.50^{+0.12}_{-0.16}$	$-30.87^{+0.17}_{-0.19}$

Table 5. Properties of the reconstructed source. From the left: magnification factor, de-magnified angular resolution and effective radius for 3σ and 5σ emission.

	μ	θ (arcsec)	$R_{\text{eff},3\sigma}$ (pc)	$R_{\text{eff},5\sigma}$ (pc)
Band 8	12.9 ± 0.2	0.02	439.02	363.1
Band 7	7.1 ± 0.1	0.08	339.3	256.3
Band 6	7.9 ± 0.1	0.09	953.01	740.8
C[II]	5.9 ± 0.3	0.04	498.7	390.4
CO(8-7)	8.1 ± 0.6	0.1	1378.3	1098.2

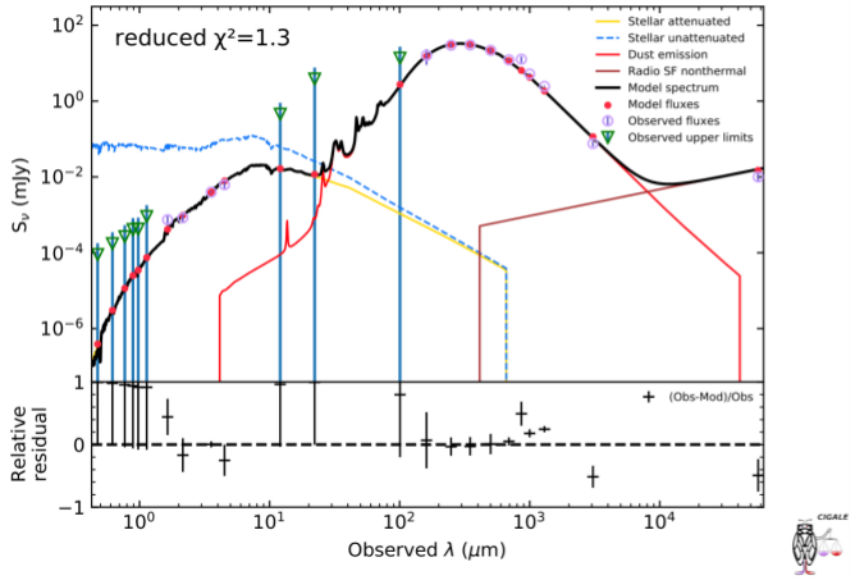


Figure 12. Best-fit UV to radio observed-frame SED of J1135. Green arrows are 3σ upper limits, purple circles are the observed flux densities and errors. The black line is the best-fitting modified black body spectrum.

Table 6. Best-fit output parameters from CIGALE. From the first row: dust luminosity, dust mass, star formation rate and stellar mass.

SED-fitting results	
$\log L_{\text{dust}} (L_{\odot})$	13.01 ± 0.06
$\log M_{\text{dust}} (M_{\odot})$	9.21 ± 0.05
$\log \text{SFR} (M_{\odot} \text{ yr}^{-1})$	2.92 ± 0.08
$\log M_{\star} (M_{\odot})$	$\lesssim 11.73$

Table 7. Values for the molecular mass computed from different calibrators.

Calibrator	$\log M_{\text{gas}} (M_{\odot})$
C[II]	11.04 ± 0.3
CO(1-0)	$\lesssim (10-10.8)$
850 μm	11.5 ± 0.2
α_{GDR}	$(10.51-11.04) \pm 0.05$

ies in literature (e.g. [Riechers et al. 2013](#)). This conversion factor is referred to a different transition, corresponding to higher luminosity values of the CO-SLED ([Yang et al. 2017](#)), for this reason the resulting value of $L'_{\text{CO}(1-0)} = 1.2 \times 10^{10} \text{ K km s}^{-1} \text{ pc}^2$ is considered as an upper limit. This estimate is consistent with the value of $L'_{\text{CO}(1-0)} \sim 1.5 \times 10^{10}$ found by [Harris et al. \(2012\)](#) adopting an indicative magnification factor of 10. We then compute the molecular gas mass assuming two different values of $\alpha_{\text{CO}} = 0.8 - 4.6$. The value of $\alpha = 0.8$ is calibrated from local ULIRGs with super-solar metallicity ([Downes & Solomon 1998](#)), while the higher value is calibrated in the Milky Way ([Solomon & Barrett 1991](#)).

The molecular gas ISM content can also be estimated by means of the empirical calibration ([Scoville et al. 2017](#)) as $\alpha \equiv < L_{\nu 850\mu\text{m}} / M_{\text{gas}} > = 6.7 \pm 1.7 \times 10^{19} \text{ erg s}^{-1} \text{ Hz}^{-1} M_{\odot}^{-1}$.

Finally, we convert the dust content resulting from the SED fitting into gas assuming a variable gas-to-dust ratio of $\delta_{\text{GDR}} = 30 - 92$ referred to typical solar and super solar metallicity following [Magdis et al. \(2012\)](#) and [Fujimoto et al. \(2022\)](#). The values obtained for the molecular gas masses are reported in Table 7.

The stellar mass estimate in output from the SED fitting must be considered as an upper limit. Indeed given the lack of a clear detection in NIR images it is not possible to correctly estimate the contribution coming from the lens (see Section 3.2 for a further discussion). Moreover, the dark-nature of this object hinders a complete sampling of the optical and NIR part of the SED. Aside from the value reported in Table 6, we compute the stellar mass assuming a typical stellar-to-dust mass ratio of

$\delta_{\text{SDR}} \approx 100$, obtaining a value of $M_{\star}^{\text{STD}} \sim 2 \times 10^{11} M_{\odot}$, in agreement with the SED fitting estimate.

6.2. ISM properties

From the gas mass values reported in Sect. 6.1, we estimate a depletion timescale of $\tau_{\text{depl}} \sim 10^8 \text{ yr}$. Moreover, the inferred stellar mass implies $\tau_{\text{SFR}} \sim 10^8 \text{ yr}$, indicative of a young galaxy, offset from the main sequence locus of star-forming galaxies at $z \sim 3$ ([Speagle et al. 2014](#)). Our results are consistent with the expectations reported in [Vishwas et al. \(2018\)](#), where the analysis of the Lyman continuum photons required to sustain the luminosity of the O[III] 88 μm line pointed out to the presence of young and massive stars ionising the surrounding HII regions. The same authors found no significant AGN contribution from the SED analysis, consistent with what we infer from the FIRRC ($q_{\text{FIR}} \approx 2.7$), which is indicative of a star-formation dominated object.

The hypothesis of J1135 being a compact starburst is also supported by the source reconstruction of the highest angular resolution ALMA continuum emission at 640 μm shown in Figure 7, where the effective radius reaches values of $\sim 400 \text{ pc}$. Similar physical scales are reached by the C[II] line emission (see Table 5 and Fig. 8). The C[II] is a fine structure line predominantly originated from high- z photon-dominated regions (PDR) and is typically used as a cool interstellar gas tracer and as a SFR estimator (see [Casey et al. 2014](#) for a review). A well known deficit in the C[II]/FIR ratio is observed in both nearby (e.g. [Luhman et al. 2003](#), [Díaz-Santos et al. 2017](#), [Smith et al. 2017](#)) and high-redshift star-forming galaxies ([Stacey et al. 2010](#), [Gullberg et al. 2015](#)). This drop is found to reach very low values ($L_{\text{C[II]}}/L_{\text{FIR}} \approx 10^{-4}$) in spatially resolved studies (e.g. [Lagache et al. 2018](#), [Gullberg et al. 2015](#), [Rybak et al. 2019](#)). For J1135, we infer a C[II]/FIR ratio of $L_{\text{C[II]}}/L_{\text{FIR}} \approx 5.4 \times 10^{-4}$. Similar values are found for other strongly lensed galaxies among the HATLAS sample. For example, [Rybak et al. \(2020\)](#) reported a deficit down to $\sim 3 \times 10^{-4}$ for spatially resolved ALMA data of SDP.81 ([Partnership et al. 2015](#), [Rybak et al. 2015a,b](#), [Dye et al. 2015](#), [Swinbank et al. 2015](#), [Tamura et al. 2015](#), [Hatsukade et al. 2015](#), [Hezaveh et al. 2016](#)) at $z = 3.042$. [Lamarche et al. \(2018\)](#) found similar values ($\sim 2 \times 10^{-4}$) for SDP.11 at $z = 1.7$, even though our galaxy shows a more compact morphology in the C[II] emission with respect to other objects. From $R_{\text{eff}, 640\mu\text{m}}$ we infer a star-formation surface density of $\rho_{\text{SFR}} \sim 1600 M_{\odot} \text{ yr}^{-1} \text{ kpc}^{-2}$, which is on the verge of the Eddington limit for a radiation pressure supported starburst ([Andrews & Thompson 2011](#), [Simpson et al. 2015](#)). This value, is compatible with the possible explanation of the

deficit to be attributed to a lower increase of the C[II] emission with respect to the FIR.

6.3. Evolutionary interpretation

By inspecting the HST/WFC3 image we find no evidence for galaxy companions of J1135 within a radius of at least ~ 5 arcsec, corresponding to ~ 40 kpc, so that we can exclude a merger-induced origin of the starburst. Thus the ISM conditions and the physical properties discussed so far can be interpreted in the light of in-situ galaxy formation scenarios (Lapi et al. 2014, 2018, Mancuso et al. 2017, Pantoni et al. 2019). In particular, the properties of J1135 are consistent with a *compaction* phase (see Fig. 3 in Lapi et al. 2018) in which the dust-enshrouded star-formation activity increases at an almost constant rate in the inner regions of the galaxy where the stellar mass is being accumulated. At this stage, the in-situ scenario envisages the galaxy to be an off-main sequence object in a early evolutionary stage, which will eventually move towards the main-sequence locus as the stellar mass content increases. Finally, the star formation will either progressively decrease as the galaxy exhaust its gas reservoir or will be abruptly stopped by the action of the feedback from an AGN (Mancuso et al. 2017).

7. SUMMARY AND CONCLUSIONS

In this work we have investigated the nature of the strongly-lensed galaxy HATLASJ113526.2-01460 (namely, J1135) at redshift $z \approx 3.1$, discovered by the *Herschel* satellite in the GAMA 12th field of the *Herschel*-ATLAS survey. We have performed detailed lens modeling and have reconstructed the source morphology in three different (sub-)mm continuum bands, and in the spectral emission of the C[II] and CO(8-7) lines. We have also exploited a wealth of photometric ancillary data to perform broadband SED-fitting and to retrieve intrinsic (i.e., corrected for magnification) physical properties. Our main findings are summarized below:

- The lens modeling indicates that the foreground lens is constituted by a (likely elliptical) galaxy with mass $\gtrsim 10^{11} M_{\odot}$ at $z \gtrsim 1.5$, while the source is found to be an optical/NIR dark, dusty star-forming galaxy whose (sub-)mm continuum and line emissions are amplified by factors $\mu \sim 6 - 13$.
- The emission of J1135 is extremely compact, with sizes $\lesssim 0.5$ kpc for the star-forming region and $\lesssim 1$ kpc for the gas component, with no clear evidence of rotation or of ongoing merging events.

- J1135 features a very high star-formation rate $\gtrsim 10^3 M_{\odot} \text{ yr}^{-1}$, that given the compact sizes is on the verge of the Eddington limit for starbursts. The radio luminosity at 6 cm from available EVLA observations is consistent with the star-formation activity, so that no significant contribution from a central AGN is emerging (see also Vishwas et al. 2018).
- J1135 is found to be extremely rich in gas $\sim 10^{11} M_{\odot}$ and dust $\gtrsim 10^9 M_{\odot}$. The stellar content $\lesssim 10^{11} M_{\odot}$ places J1135 well above the main sequence of starforming galaxies, indicating that the starburst is rather young with an estimated age $\sim 10^8$ yr, and that the stellar mass should at least double before star formation is quenched.
- The properties of J1135 can be consistently explained in terms of in-situ galaxy formation and evolution scenarios as typical of a rather young dusty starforming galaxy caught in the compaction phase.

In the next future, observations coming from the James Webb Space Telescope (JWST) will be crucial to shed further light on the nature of this obscured object and its foreground lens in the near- and mid-IR regime. Moreover, X-Ray follow-up, coupled with the available ALMA data, are required to establish the presence of the dust-enshrouded AGN and to better investigate the interplay between star-formation and the nuclear activity (Massardi et al. 2017).

8. ACKNOWLEDGMENTS

This paper makes use of the following ALMA data: 2016.1.01371, 2017.1.01694.S, 2018.1.00861.S. ALMA is a partnership of ESO (representing its member states), NSF (USA) and NINS (Japan), together with NRC (Canada), MOST and ASIAA (Taiwan), and KASI (Republic of Korea), in cooperation with the Republic of Chile. The Joint ALMA Observatory is operated by ESO, AUI/NRAO and NAOJ. We acknowledge financial support from the grant PRIN MIUR 2017 prot. 20173ML3WW 001 and 002 ‘Opening the ALMA window on the cosmic evolution of gas, stars, and super-massive black holes’. AL is supported by the EU H2020-MSCAITN-2019 project 860744 ‘BiD4BEST: Big Data applications for Black hole Evolution Studies’.

APPENDIX

A. ADAPTING THE SLI METHOD TO INTERFEROMETRIC VISIBILITIES

The SLI formalism can be extended also to interferometry (Dye et al. 2018, Enia et al. 2018, Maresca et al. 2022), modeling a set of visibility data, i.e. the result of the correlation of signals coming from an astrophysical source and collected by the antennae array, whose Fourier transform gives the source surface brightness distribution. Performing an inversion directly on the Fourier space (or uv -plane) circumvents the issue of dealing with artifacts and noise correlation arising in the image as a consequence of a poor sampling of the uv -plane.

Following a similar formalism with respect to the one used in Dye et al. (2018), we introduce the rectangular matrix f_{ij} containing the fluxes of the i -th pixel in the source plane and the respective j -th image-plane pixel. Analogously, complex visibilities from the lensed image are collected rectangular matrix g_{ij} , which are the Fourier transform of the i source pixels in unit surface brightness computed at the j -th visibility point in the uv -plane. For each j -th visibility corresponding to the source pixel surface brightnesses s_i , the model visibility set can be described as $\sum_i s_i g_{ij}$.

Given a set of observed visibilities V_{obs} , the merit function can be described as:

$$G = \frac{1}{2}\chi^2 = \frac{1}{2} \sum_{j=1}^J \left(\frac{\left| \sum_{i=1}^I s_i g_{ij} - V_{obs,j} \right|^2}{\sigma_j^2} \right) + \lambda \frac{1}{2} \mathbf{S}^T \mathbf{H} \mathbf{S}, \quad (\text{A1})$$

computed over a total of I Delaunay pixels and J visibilities. σ_j are the 1σ uncertainties on the observed visibilities rescaled adopting the CASA task `statwt` to match their absolute value. The last term in the expression describes the *regularization*, where λ is a constant determining the strength of the regularization, and \mathbf{H} the regularization matrix. The values s_i , represented by the vector \mathbf{S} which best reproduces the observed image-plane visibilities, can therefore be derived minimizing the merit function G . The solution to this linear problem is given by:

$$\mathbf{S} = [\mathbf{F} + \lambda \mathbf{H}]^{-1} \mathbf{D}, \quad (\text{A2})$$

where \mathbf{F} and \mathbf{D} are respectively the matrices $F_{ij} = \sum_{n=1}^J (g_{in}^{\mathbb{R}} g_{jn}^{\mathbb{R}} + g_{in}^{\mathbb{I}} g_{jn}^{\mathbb{I}} / \sigma_n^2)$ and $D_i = \sum_{n=1}^J (g_{in}^{\mathbb{R}} V_n^{\mathbb{R}} + g_{in}^{\mathbb{I}} V_n^{\mathbb{I}} / \sigma_n^2)$.

For a fixed mass model, the image plane pixels are traced back to the source plane and grouped together by means of a k-clustering algorithm, comparing each source-pixel with the neighbors sharing a direct vertex. This procedure results in new source plane's centres, used to trace a Delaunay grid. When dealing with a large number of visibilities, the computational efficiency and the memory costs are greatly improved by performing non-uniform Fast Fourier Transform (NUFFT) algorithm, implemented in `PyAutoLens` exploiting the `PyNUFFT` (Lin 2018) library and the linear algebra package `PyLops` (Ravasi & Vasconcelos 2020).

REFERENCES

- | | |
|--|---|
| <p>Aihara, H., Armstrong, R., Bickerton, S., et al. 2018, PASJ, 70, S8, doi: 10.1093/pasj/psx081</p> <p>Aihara, H., AlSayyad, Y., Ando, M., et al. 2022, PASJ, doi: 10.1093/pasj/psab122</p> <p>Andreani, P., Retana-Montenegro, E., Zhang, Z.-Y., et al. 2018, A&A, 615, A142, doi: 10.1051/0004-6361/201732560</p> <p>Andrews, B. H., & Thompson, T. A. 2011, ApJ, 727, 97, doi: 10.1088/0004-637X/727/2/97</p> <p>Aravena, M., Decarli, R., Walter, F., et al. 2016, ApJ, 833, 71, doi: 10.3847/1538-4357/833/1/71</p> <p>Bakx, T. J. L. C., Eales, S. A., Negrello, M., et al. 2018, MNRAS, 473, 1751, doi: 10.1093/mnras/stx2267</p> | <p>Becker, R. H., White, R. L., & Helfand, D. J. 1995, ApJ, 450, 559, doi: 10.1086/176166</p> <p>Blain, A. W. 1996, MNRAS, 283, 1340, doi: 10.1093/mnras/283.4.1340</p> <p>Boquien, M., Burgarella, D., Roehlly, Y., et al. 2019, A&A, 622, A103, doi: 10.1051/0004-6361/201834156</p> <p>Bruzual, G., & Charlot, S. 2003, MNRAS, 344, 1000, doi: 10.1046/j.1365-8711.2003.06897.x</p> <p>Bussmann, R. S., Pérez-Fournon, I., Amber, S., et al. 2013, ApJ, 779, 25, doi: 10.1088/0004-637X/779/1/25</p> <p>Calanog, J. A., Fu, H., Cooray, A., et al. 2014, ApJ, doi: 10.1088/0004-637X/797/2/138</p> |
|--|---|

- Carilli, C. L., & Walter, F. 2013, *ARA&A*, 51, 105, doi: [10.1146/annurev-astro-082812-140953](https://doi.org/10.1146/annurev-astro-082812-140953)
- Casey, C. M., Narayanan, D., & Cooray, A. 2014, *PhR*, 541, 45, doi: [10.1016/j.physrep.2014.02.009](https://doi.org/10.1016/j.physrep.2014.02.009)
- Chabrier, G. 2003, *PASP*, 115, 763, doi: [10.1086/376392](https://doi.org/10.1086/376392)
- Charlot, S., & Fall, S. M. 2000, *ApJ*, 539, 718, doi: [10.1086/309250](https://doi.org/10.1086/309250)
- de Jong, J. T. A., Kuijken, K., Applegate, D., et al. 2013, *The Messenger*, 154, 44
- Díaz-Santos, T., Armus, L., Charmandaris, V., et al. 2017, *ApJ*, 846, 32, doi: [10.3847/1538-4357/aa81d7](https://doi.org/10.3847/1538-4357/aa81d7)
- Downes, D., & Solomon, P. M. 1998, *ApJ*, 507, 615, doi: [10.1086/306339](https://doi.org/10.1086/306339)
- Draine, B. T., & Li, A. 2007, *ApJ*, 657, 810, doi: [10.1086/511055](https://doi.org/10.1086/511055)
- Draine, B. T., Aniano, G., Krause, O., et al. 2014, *ApJ*, 780, 172, doi: [10.1088/0004-637X/780/2/172](https://doi.org/10.1088/0004-637X/780/2/172)
- Dudzevičiūtė, U., Smail, I., Swinbank, A. M., et al. 2020, *MNRAS*, 494, 3828, doi: [10.1093/mnras/staa769](https://doi.org/10.1093/mnras/staa769)
- Dunlop, J. S., McLure, R. J., Biggs, A. D., et al. 2017, *MNRAS*, 466, 861, doi: [10.1093/mnras/stw3088](https://doi.org/10.1093/mnras/stw3088)
- Dye, S., Furlanetto, C., Swinbank, A. M., et al. 2015, *MNRAS*, 452, 2258, doi: [10.1093/mnras/stv1442](https://doi.org/10.1093/mnras/stv1442)
- Dye, S., Furlanetto, C., Dunne, L., et al. 2018, *MNRAS*, 476, 4383, doi: [10.1093/mnras/sty513](https://doi.org/10.1093/mnras/sty513)
- Dye, S., Eales, S. A., Gomez, H. L., et al. 2022, *MNRAS*, 510, 3734, doi: [10.1093/mnras/stab3569](https://doi.org/10.1093/mnras/stab3569)
- Eales, S., Dunne, L., Clements, D., et al. 2010, *PASP*, 122, 499, doi: [10.1086/653086](https://doi.org/10.1086/653086)
- Edge, A., Sutherland, W., Kuijken, K., et al. 2013, *The Messenger*, 154, 32, <https://ui.adsabs.harvard.edu/abs/2013Msngr.154...32E>
- Enia, A., Negrello, M., Gurwell, M., et al. 2018, *MNRAS*, 475, 3467, doi: [10.1093/mnras/sty021](https://doi.org/10.1093/mnras/sty021)
- Enia, A., Talia, M., Pozzi, F., et al. 2022, *ApJ*, 927, 204, doi: [10.3847/1538-4357/ac51ca](https://doi.org/10.3847/1538-4357/ac51ca)
- Franco, M., Elbaz, D., Béthermin, M., et al. 2018, *A&A*, 620, A152, doi: [10.1051/0004-6361/201832928](https://doi.org/10.1051/0004-6361/201832928)
- Fujimoto, S., Brammer, G. B., Watson, D., et al. 2022, *Nature*, 604, 261, doi: [10.1038/s41586-022-04454-1](https://doi.org/10.1038/s41586-022-04454-1)
- Gruppioni, C., Béthermin, M., Loiacono, F., et al. 2020, *A&A*, 643, A8, doi: [10.1051/0004-6361/202038487](https://doi.org/10.1051/0004-6361/202038487)
- Gullberg, B., De Breuck, C., Vieira, J. D., et al. 2015, *MNRAS*, 449, 2883, doi: [10.1093/mnras/stv372](https://doi.org/10.1093/mnras/stv372)
- Harris, A. I., Baker, A. J., Frayer, D. T., et al. 2012, *ApJ*, 752, 152, doi: [10.1088/0004-637X/752/2/152](https://doi.org/10.1088/0004-637X/752/2/152)
- Hatsukade, B., Tamura, Y., Iono, D., et al. 2015, *PASJ*, 67, 93, doi: [10.1093/pasj/psv061](https://doi.org/10.1093/pasj/psv061)
- Hatsukade, B., Kohno, K., Yamaguchi, Y., et al. 2018, *PASJ*, 70, 105, doi: [10.1093/pasj/psy104](https://doi.org/10.1093/pasj/psy104)
- Hezaveh, Y. D., Dalal, N., Marrone, D. P., et al. 2016, *ApJ*, 823, 37, doi: [10.3847/0004-637X/823/1/37](https://doi.org/10.3847/0004-637X/823/1/37)
- Kormann, R., Schneider, P., & Bartelmann, M. 1994, *A&A*, 284, 285, <https://ui.adsabs.harvard.edu/abs/1994A&A...284..285K>
- Lagache, G., Cousin, M., & Chatzikos, M. 2018, *A&A*, 609, A130, doi: [10.1051/0004-6361/201732019](https://doi.org/10.1051/0004-6361/201732019)
- Lamarche, C., Verma, A., Vishwas, A., et al. 2018, *ApJ*, 867, 140, doi: [10.3847/1538-4357/aac394](https://doi.org/10.3847/1538-4357/aac394)
- Lapi, A., Negrello, M., González-Nuevo, J., et al. 2012, *ApJ*, 755, 46, doi: [10.1088/0004-637X/755/1/46](https://doi.org/10.1088/0004-637X/755/1/46)
- Lapi, A., Raimundo, S., Aversa, R., et al. 2014, *ApJ*, 782, 69, doi: [10.1088/0004-637X/782/2/69](https://doi.org/10.1088/0004-637X/782/2/69)
- Lapi, A., Pantoni, L., Zanisi, L., et al. 2018, *Astrophys. J.* 857 (2018), 22, doi: [10.3847/1538-4357/aab6af](https://doi.org/10.3847/1538-4357/aab6af)
- Lawrence, A., Warren, S. J., Almaini, O., et al. 2007, *MNRAS*, 379, 1599, doi: [10.1111/j.1365-2966.2007.12040.x](https://doi.org/10.1111/j.1365-2966.2007.12040.x)
- Lin, J.-M. 2018, *Journal of Imaging*, 4, doi: [10.3390/jimaging4030051](https://doi.org/10.3390/jimaging4030051)
- Luhman, M. L., Satyapal, S., Fischer, J., et al. 2003, *ApJ*, 594, 758, doi: [10.1086/376965](https://doi.org/10.1086/376965)
- Ma, B., Cooray, A., Calanog, J. A., et al. 2015, *ApJ*, 814, 17, doi: [10.1088/0004-637X/814/1/17](https://doi.org/10.1088/0004-637X/814/1/17)
- Maddox, S. J., Valiante, E., Cigan, P., et al. 2017, *ApJ*, doi: [10.3847/1538-4365/aab8fc](https://doi.org/10.3847/1538-4365/aab8fc)
- Magdis, G. E., Daddi, E., Béthermin, M., et al. 2012, *ApJ*, 760, 6, doi: [10.1088/0004-637X/760/1/6](https://doi.org/10.1088/0004-637X/760/1/6)
- Mancuso, C., Lapi, A., Massardi, M., & Danese, L. 2017, in *Workshop sull'Astronomia Millimetrica in Italia*, 2, doi: [10.5281/zenodo.1048809](https://doi.org/10.5281/zenodo.1048809)
- Maresca, J., Dye, S., Amvrosiadis, A., et al. 2022, *MNRAS*, doi: [10.1093/mnras/stac585](https://doi.org/10.1093/mnras/stac585)
- Marrone, D. P., Spilker, J. S., Hayward, C. C., et al. 2018, *Nature*, 553, 51, doi: [10.1038/nature24629](https://doi.org/10.1038/nature24629)
- Massardi, M., Enia, A. F. M., Negrello, M., et al. 2017, *A&A*, doi: [10.1051/0004-6361/201731751](https://doi.org/10.1051/0004-6361/201731751)
- Nayyeri, H., Keele, M., Cooray, A., et al. 2016, *ApJ*, 823, 17, doi: [10.3847/0004-637X/823/1/17](https://doi.org/10.3847/0004-637X/823/1/17)
- Negrello, M., Hopwood, R., De Zotti, G., et al. 2010, *Science*, 330, 800, doi: [10.1126/science.1193420](https://doi.org/10.1126/science.1193420)
- Negrello, M., Hopwood, R., Dye, S., et al. 2014, *MNRAS*, 440, 1999, doi: [10.1093/mnras/stu413](https://doi.org/10.1093/mnras/stu413)
- Negrello, M., Amber, S., Amvrosiadis, A., et al. 2017, *MNRAS*, 465, 3558, doi: [10.1093/mnras/stw2911](https://doi.org/10.1093/mnras/stw2911)
- Nightingale, J., Hayes, R., Kelly, A., et al. 2021, *The Journal of Open Source Software*, 6, 2825, doi: [10.21105/joss.02825](https://doi.org/10.21105/joss.02825)
- Nightingale, J. W., & Dye, S. 2015, *MNRAS*, 452, 2940, doi: [10.1093/mnras/stv1455](https://doi.org/10.1093/mnras/stv1455)

- Nightingale, J. W., Dye, S., & Massey, R. J. 2018, MNRAS, 478, 4738, doi: [10.1093/mnras/sty1264](https://doi.org/10.1093/mnras/sty1264)
- Oliver, S. J., Bock, J., Altieri, B., et al. 2012, MNRAS, 424, 1614, doi: [10.1111/j.1365-2966.2012.20912.x](https://doi.org/10.1111/j.1365-2966.2012.20912.x)
- Pantoni, L., Lapi, A., Massardi, M., Goswami, S., & Danese, L. 2019, ApJ, 880, 129, doi: [10.3847/1538-4357/ab2adc](https://doi.org/10.3847/1538-4357/ab2adc)
- Pantoni, L., Massardi, M., Lapi, A., et al. 2021, MNRAS, doi: [10.1093/mnras/stab2346](https://doi.org/10.1093/mnras/stab2346)
- Partnership, A., Vlahakis, C., Hunter, T. R., et al. 2015, ApJL, 808, L4, doi: [10.1088/2041-8205/808/1/L4](https://doi.org/10.1088/2041-8205/808/1/L4)
- Planck Collaboration, Aghanim, N., Akrami, Y., et al. 2020, A&A, 641, A6, doi: [10.1051/0004-6361/201833910](https://doi.org/10.1051/0004-6361/201833910)
- Polletta, M., Tajer, M., Maraschi, L., et al. 2007, ApJ, 663, 81, doi: [10.1086/518113](https://doi.org/10.1086/518113)
- Ravasi, M., & Vasconcelos, I. 2020, SoftwareX, 11, 100361, doi: <https://doi.org/10.1016/j.softx.2019.100361>
- Riechers, D. A., Bradford, C. M., Clements, D. L., et al. 2013, Nature, 496, 329, doi: [10.1038/nature12050](https://doi.org/10.1038/nature12050)
- Riechers, D. A., Hodge, J. A., Pavesi, R., et al. 2020, ApJ, 895, 81, doi: [10.3847/1538-4357/ab8c48](https://doi.org/10.3847/1538-4357/ab8c48)
- Rybak, M., Hodge, J. A., Vegetti, S., et al. 2020, MNRAS, 494, 5542, doi: [10.1093/mnras/staa879](https://doi.org/10.1093/mnras/staa879)
- Rybak, M., McKean, J. P., Vegetti, S., Andreani, P., & White, S. D. M. 2015a, MNRAS, 451, L40, doi: [10.1093/mnras/slv058](https://doi.org/10.1093/mnras/slv058)
- Rybak, M., Vegetti, S., McKean, J. P., Andreani, P., & White, S. D. M. 2015b, MNRAS, 453, L26, doi: [10.1093/mnras/slv092](https://doi.org/10.1093/mnras/slv092)
- Rybak, M., Calistro Rivera, G., Hodge, J. A., et al. 2019, ApJ, 876, 112, doi: [10.3847/1538-4357/ab0e0f](https://doi.org/10.3847/1538-4357/ab0e0f)
- Scoville, N., Lee, N., Vanden Bout, P., et al. 2017, ApJ, 837, 150, doi: [10.3847/1538-4357/aa61a0](https://doi.org/10.3847/1538-4357/aa61a0)
- Shu, X., Yang, L., Liu, D., et al. 2022, ApJ, 926, 155, doi: [10.3847/1538-4357/ac3de5](https://doi.org/10.3847/1538-4357/ac3de5)
- Simpson, J. M., Smail, I., Swinbank, A. M., et al. 2015, ApJ, 799, 81, doi: [10.1088/0004-637X/799/1/81](https://doi.org/10.1088/0004-637X/799/1/81)
- Simpson, J. M., Smail, I., Dudzevičiūtė, U., et al. 2020, MNRAS, 495, 3409, doi: [10.1093/mnras/staa1345](https://doi.org/10.1093/mnras/staa1345)
- Smith, J. D. T., Croxall, K., Draine, B., et al. 2017, ApJ, 834, 5, doi: [10.3847/1538-4357/834/1/5](https://doi.org/10.3847/1538-4357/834/1/5)
- Solomon, P. M., & Barrett, J. W. 1991, in Dynamics of Galaxies and Their Molecular Cloud Distributions, ed. F. Combes & F. Casoli, Vol. 146, 235. <https://ui.adsabs.harvard.edu/abs/1991IAUS..146..235S>
- Speagle, J. S. 2020, MNRAS, 493, 3132, doi: [10.1093/mnras/staa278](https://doi.org/10.1093/mnras/staa278)
- Speagle, J. S., Steinhardt, C. L., Capak, P. L., et al. 2014, in American Astronomical Society Meeting Abstracts, Vol. 223, American Astronomical Society Meeting Abstracts #223, 246.44. <https://ui.adsabs.harvard.edu/abs/2014AAS...22324644S>
- Stacey, G. J., Hailey-Dunsheath, S., Ferkinhoff, C., et al. 2010, ApJ, 724, 957, doi: [10.1088/0004-637X/724/2/957](https://doi.org/10.1088/0004-637X/724/2/957)
- Swinbank, A. M., Dye, S., Nightingale, J. W., et al. 2015, ApJL, 806, L17, doi: [10.1088/2041-8205/806/1/L17](https://doi.org/10.1088/2041-8205/806/1/L17)
- Talia, M., Cimatti, A., Giuliotti, M., et al. 2021, ApJ, 909, 23, doi: [10.3847/1538-4357/abd6e3](https://doi.org/10.3847/1538-4357/abd6e3)
- Tamura, Y., Oguri, M., Iono, D., et al. 2015, PASJ, 67, 72, doi: [10.1093/pasj/psv040](https://doi.org/10.1093/pasj/psv040)
- Valiante, E., Smith, M. W. L., Eales, S., et al. 2016, MNRAS, doi: [10.1093/mnras/stw1806](https://doi.org/10.1093/mnras/stw1806)
- Viero, M. P., Asboth, V., Roseboom, I. G., et al. 2014, ApJS, 210, 22, doi: [10.1088/0067-0049/210/2/22](https://doi.org/10.1088/0067-0049/210/2/22)
- Vishwas, A., Ferkinhoff, C., Nikola, T., et al. 2018, ApJ, 856, 174, doi: [10.3847/1538-4357/aab354](https://doi.org/10.3847/1538-4357/aab354)
- Walter, F., Decarli, R., Aravena, M., et al. 2016, ApJ, 833, 67, doi: [10.3847/1538-4357/833/1/67](https://doi.org/10.3847/1538-4357/833/1/67)
- Wang, T., Elbaz, D., Schreiber, C., et al. 2016, ApJ, 816, 84, doi: [10.3847/0004-637X/816/2/84](https://doi.org/10.3847/0004-637X/816/2/84)
- Wang, T., Schreiber, C., Elbaz, D., et al. 2019, Nature, 572, 211, doi: [10.1038/s41586-019-1452-4](https://doi.org/10.1038/s41586-019-1452-4)
- Ward, B. A., Eales, S. A., Pons, E., et al. 2022, MNRAS, 510, 2261, doi: [10.1093/mnras/stab3300](https://doi.org/10.1093/mnras/stab3300)
- Wardlow, J. L., Cooray, A., De Bernardis, F., et al. 2013, ApJ, 762, 59, doi: [10.1088/0004-637X/762/1/59](https://doi.org/10.1088/0004-637X/762/1/59)
- Warren, S. J., & Dye, S. 2003, ApJ, 590, 673, doi: [10.1086/375132](https://doi.org/10.1086/375132)
- Williams, C. C., Labbe, I., Spilker, J., et al. 2019, ApJ, 884, 154, doi: [10.3847/1538-4357/ab44aa](https://doi.org/10.3847/1538-4357/ab44aa)
- Wright, E. L., Eisenhardt, P. R. M., Mainzer, A. K., et al. 2010, AJ, 140, 1868, doi: [10.1088/0004-6256/140/6/1868](https://doi.org/10.1088/0004-6256/140/6/1868)
- Yang, C., Omont, A., Beelen, A., et al. 2017, A&A, 608, A144, doi: [10.1051/0004-6361/201731391](https://doi.org/10.1051/0004-6361/201731391)
- Zanella, A., Daddi, E., Magdis, G., et al. 2018, MNRAS, 481, 1976, doi: [10.1093/mnras/sty2394](https://doi.org/10.1093/mnras/sty2394)